

Robustness of competing climatic states

Article

Published Version

Creative Commons: Attribution 4.0 (CC-BY)

Open access

Ragon, C., Lembo, V., Lucarini, V. ORCID:
<https://orcid.org/0000-0001-9392-1471>, Verard, C., Kasparian,
J. and Brunetti, M. (2022) Robustness of competing climatic
states. *Journal of Climate*, 35 (9). pp. 2769-2784. ISSN 1520-
0442 doi: 10.1175/JCLI-D-21-0148.1 Available at
<https://centaur.reading.ac.uk/102510/>

It is advisable to refer to the publisher's version if you intend to cite from the
work. See [Guidance on citing](#).

To link to this article DOI: <http://dx.doi.org/10.1175/JCLI-D-21-0148.1>

Publisher: American Meteorological Society

All outputs in CentAUR are protected by Intellectual Property Rights law,
including copyright law. Copyright and IPR is retained by the creators or other
copyright holders. Terms and conditions for use of this material are defined in
the [End User Agreement](#).

www.reading.ac.uk/centaur

CentAUR

Central Archive at the University of Reading

Reading's research outputs online

Robustness of Competing Climatic States

CHARLINE RAGON,^a VALERIO LEMBO,^b VALERIO LUCARINI,^{c,d} CHRISTIAN VÉRARD,^e JÉRÔME KASPARIAN,^a
AND MAURA BRUNETTI^a

^a Group of Applied Physics and Institute for Environmental Sciences, University of Geneva, Geneva, Switzerland

^b Institute of Atmospheric Sciences and Climate, Consiglio Nazionale delle Ricerche, ISAC-CNR, Bologna, Italy

^c Department of Mathematics and Statistics, University of Reading, Reading, United Kingdom

^d Centre for the Mathematics of Planet Earth, University of Reading, Reading, United Kingdom

^e Section of Earth and Environmental Sciences, University of Geneva, Geneva, Switzerland

(Manuscript received 22 February 2021, in final form 24 November 2021)

ABSTRACT: The climate is a nonequilibrium system undergoing the continuous action of forcing and dissipation. Under the effect of a spatially inhomogeneous absorption of solar energy, all the climate components dynamically respond until an approximate steady state (or attractor) is reached. However, multiple steady states can coexist for a given forcing and with the same boundary conditions. Here, we apply the Thermodynamic Diagnostic Tool (TheDiaTo) to investigate the statistical properties of five coexisting climates, ranging from a snowball to an ice-free aquaplanet, obtained in MITgcm coupled simulations. The aim is to explore the multistability of the climate model setup by highlighting differences in competing steady states and their characteristic signatures regarding the meridional transport of heat and water mass, the Lorenz energy cycle, and the material entropy production. We also investigate how such attractors change when the model configuration is varied. We consider, in particular, the effect of changing the representation of the cloud albedo, and of implementing an improved closure of the energy budget. We find that, even if the dynamics remain on the same attractor, state variables are modified. The set of metrics in TheDiaTo quantifies such modifications and represents a valuable tool for model evaluation.


KEYWORDS: Energy transport; Climate classification/regimes; Statistics; General circulation models


1. Introduction

The climate is a highly complex and heterogeneous nonequilibrium system undergoing the continuous action of forcing and dissipation. The main source of external forcing is the inhomogeneous absorption of incoming solar radiation. The atmosphere dynamically responds to such energy input by redistributing the heat from lower to higher values of both latitudes and altitudes (Peixoto and Oort 1992; Lucarini et al. 2014; Ghil and Lucarini 2020). On the other hand, the ocean is essentially fueled by winds, tides, and buoyancy forcing (Munk and Wunsch 1998; Wunsch and Ferrari 2004). As a result, the inhomogeneous absorption of solar heat triggers a complex set of instabilities and feedbacks occurring at a wide range of temporal and spatial scales, redistributing heat and water mass, until approximate steady-state conditions are achieved (Peixoto and Oort 1992) where the dynamics of the system lies upon a high-dimensional attractor (Saltzman 2001; Lucarini et al. 2014; Ghil and Lucarini 2020).

A generally accepted theoretical framework is that the climate is a multistable dynamical system, where multiple competing

attractors can coexist under the same forcing and boundary conditions (Budyko 1969; Sellers 1969; Ghil 1976; Saltzman 2001; Ghil and Lucarini 2020). This implies that the phase space is partitioned among the basins of attraction corresponding to the various attractors and the basin boundaries (Lucarini and Bódai 2017). Transition between the competing steady states is possible if the system undergoes forcing of deterministic or stochastic nature (Saltzman 2001; Ghil and Lucarini 2020; Margazoglou et al. 2021). As an example, observational evidence suggests that during the Neoproterozoic era our planet flipped in and out of a so-called snowball state (Hoffman et al. 1998; Pierrehumbert et al. 2011). Multistability reflects the fact that there are different manners to redistribute the energy among the climate components in such a way that a stable climate can be established. It has been detected in models of different complexity, from energy balance models (Budyko 1969; Sellers 1969; Ghil 1976; Abbot et al. 2011) and general circulation models (GCMs) coupled to slab oceans (Lucarini et al. 2010; Boschi et al. 2013; Popp et al. 2016; Lucarini and Bódai 2017; Lucarini and Bódai 2019; Lucarini and Bódai 2020) to fully coupled GCMs (Ferreira et al. 2011; Rose 2015). All these models have been able to reproduce the dichotomy between the competing warm and snowball climates. Indeed, modeling exercises indicate the possible existence of additional climatic configurations, such as the slushball Earth (Lewis et al. 2007) and the Jormungand state (Abbot et al. 2011).

 Denotes content that is immediately available upon publication as open access.

 Supplemental information related to this paper is available at the Journals Online website: <https://doi.org/10.1175/JCLI-D-21-0148.s1>.

Corresponding author: M. Brunetti, maura.brunetti@unige.ch



This article is licensed under a Creative Commons Attribution 4.0 license (<http://creativecommons.org/licenses/by/4.0/>).

Recently, up to five attractors were found to coexist under the same forcing and boundary conditions using the MIT general circulation model (MITgcm) (Marshall et al. 1997a,b; Adcroft et al. 2004; Marshall et al. 2004) in a coupled aquaplanet configuration (Brunetti et al. 2019). In terms of average surface temperature, these attractors range from the usual snowball state, which is completely covered by ice, to a hot, ice-free state, which is warmer than the usual warm state found in other studies. How can this large variety of coexisting states be physically described in a manner that sets the different states apart? To address this issue, we extend the analysis of such attractors performed in Brunetti et al. (2019) with the construction of the entire bifurcation diagram for a solar constant ranging between 1336 and 1400 W m⁻² and with the addition of, in particular, two new metrics, the intensity of the Lorenz energy cycle (LEC) and the material entropy production (MEP) of the atmosphere.

The extended set of metrics used to characterize the multiple attractors can furthermore be used to quantify biases in climate models, an important instrument for the understanding of climate dynamics (Eyring et al. 2016; Balaji et al. 2017). Despite the impressive progress in last decades, biases still remain in the new generation of climate models that are extremely difficult to reduce (Wang et al. 2014; Rauser et al. 2015; Zhang et al. 2015; Palmer 2016; Stouffer et al. 2017; McKenna et al. 2020; Liao et al. 2021). Such biases affect the description of key climatic features like the interplay of global modes of variability (Yang et al. 2018), their magnitude and frequency, or the occurrence of extremes (Perkins 2011), and reveal the limits of our ability to correctly reproduce the response to external (solar) or internal (volcanic and anthropogenic) forcings (Rose et al. 2013; Gupta et al. 2019).

A main source of biases in climate models comes from the use of parameterizations of unresolved processes. In addition to the use of insufficiently observationally constrained parameters, parameterizations are often not constrained to conservation properties (Anthes 1985; Hourdin et al. 2016). This can have an impact on the mean properties of the modeled system, inducing numerical drifts, and deserves particular attention. Here, we will focus specifically on two examples, by looking at the effect of different prescriptions for the cloud albedo and at the effect of improving the global energy budget of the model, to show the utility of considering a set of metrics including LEC and MEP.

To characterize the different attractors and address model biases in a comprehensive manner we use the Thermodynamic Diagnostic Tool (TheDiaTo; Lembo et al. 2019). TheDiaTo is a software tool that calculates a large set of metrics, including the aforementioned ones, and is thus ideally suited for the task at hand. TheDiaTo is also part of the CMIP6 ESMValTool 2.0 Earth system models diagnostic community effort (Eyring et al. 2020).

The paper is organized as follows. After the description of our setups and simulations used to construct the bifurcation diagram in section 2, we apply TheDiaTo in section 3 to study the five competing attractors. In section 4, we discuss how reinjecting dissipated kinetic energy affects the physical budgets and the overall properties of the attractors, focusing on the hot state. In section 5, we investigate the impact of changing the cloud

albedo scheme on what we refer later to as the cold state, which is intermediate with respect to surface temperature. Finally, we discuss the importance of performing such diagnostics in climate models before drawing our conclusions in section 6.

2. Methods and simulation setups

The simulations are performed using the MIT global circulation model (MITgcm, version c65q; Marshall et al. (1997a,b); Adcroft et al. (2004)), a coupled atmosphere–ocean–sea ice model with a 15-level dynamical ocean, a thermodynamic module for the sea ice component (Winton 2000), and a 5-layer atmospheric radiative module based on the SPEEDY model (Molteni 2003). The top layer represents the stratosphere, the bottom one the planetary boundary layer, and the remaining three the free troposphere. SPEEDY is an atmospheric module of intermediate complexity that provides a rather realistic representation of the flow despite the coarse vertical resolution and the simplified physical parameterizations, as results from the comparisons with ERA and NCEP–NCAR reanalysis fields (Molteni 2003), with the advantage of requiring less computer resources than state-of-the-art atmospheric models.

MITgcm is run in an aquaplanet configuration with no continents. The same dynamical kernel is used for both the ocean and the atmosphere, which are represented over the same cubed-sphere grid (Marshall et al. 2004). Each face of the cube includes 32×32 cells, corresponding to an average horizontal resolution of 2.8°. The ocean depth is set to a fixed value of 3000 m. The CO₂ concentration in the atmosphere is set to 326 ppm and various values for the solar irradiance S_0 are considered, as detailed below. The orbital forcing is prescribed at present-day values, so seasonality is taken into account. Albedos for snow, ice, and ocean surface are within the observed range and correspond to those used in Brunetti et al. (2019). The relative humidity threshold for the formation of low clouds, a parameter denoted as RHCL2 in MITgcm, is set to the same value for all the simulations considered in the present study, RHCL2 = 0.7239.

We extend the analysis performed in Brunetti et al. (2019) by running 28 additional simulations with different incoming solar radiation S_0 . This allows us to construct the bifurcation diagram¹ where the mean surface air temperature on the attractors is plotted as a function of the incoming solar radiation in the range $S_0 = 334\text{--}350$ W m⁻², as shown in Fig. 1 (green triangles). The bifurcation diagram is of critical importance to determine the range of stability of each attractor within a given model setup, and to define multistability regions. To find the stable branches (solid lines), the simulations are initialized from the five competing attractors found in Brunetti et al. (2019) at $S_0 = 342$ W m⁻² with slightly different values of incoming solar radiation, and this procedure is repeated until a tipping point is reached, where a shift to a different attractor is observed. We take the pragmatic approach of assuming that statistically steady-state conditions are

¹ Other bifurcation diagrams obtained with MITgcm with an horizontal resolution of 3.75° and simplified continental configurations can be found in Rose (2015) and Gupta et al. (2019).

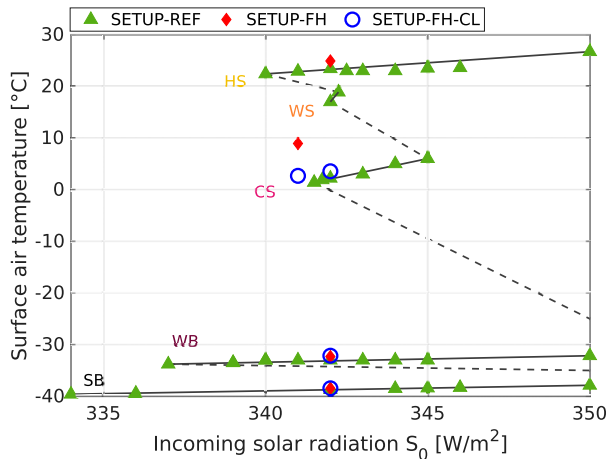


FIG. 1. Bifurcation diagram for SETUP-REF (green triangles). Solid lines correspond to stable branches, while dashed lines correspond to qualitative sketches of unstable branches. Diamonds and circles denote the attractors for SETUP-FH and SETUP-FH-CL, respectively.

realized within each attractor when its mean annual surface energy balance F_s becomes lower than 0.2 W m^{-2} in absolute value, corresponding to an ocean temperature drift $dT/dt = F_s/(c_p \rho h)$ (Marshall and Plumb 2008, p. 229) lower than $0.05^\circ\text{C century}^{-1}$, with $c_p = 4000 \text{ J K}^{-1} \text{ kg}^{-1}$ being the specific heat capacity, $\rho = 1023 \text{ kg m}^{-3}$ the seawater density, and $h = 3000 \text{ m}$ the ocean depth. Indeed, under such conditions, we see virtually no drift in the annual averages of the climatic observables of interest. Five stable branches exist, corresponding to the following climates: hot state (HS), warm state (WS), cold state (CS), waterbelt (WB), and snowball (SB). In particular, WS is stable within a narrow range of values of the solar constant,² $1368\text{--}1370 \text{ W m}^{-2}$, while SB is stable for all the tested values ranging from 1336 to 1400 W m^{-2} .

The bifurcation diagram is obtained using the reference model setup where the dissipated kinetic energy is not reinjected in the system and low-cloud albedo is fixed to the constant value $\alpha_{c0} = 0.38$. This is denoted as SETUP-REF [and corresponds to SetUp2 in Brunetti et al. (2019)]. We then alter one process at a time to better understand the impact of such changes on the model's performance. In SETUP-FH, the dissipated kinetic energy is reinjected into the system as thermal energy (see section 4; red diamonds in Fig. 1). This is achieved by means of a flag available in MITgcm, allowing us to locally calculate the dissipated kinetic energy at each grid point and vertical level, except the top one representing the stratosphere, and to reinject it each time step as a contribution to the forcing term in the tendency equation for the temperature. In the last considered setup, denoted as SETUP-FH-CL (see section 5), we also include a dependence of cloud albedo on latitude

² Green triangles are not regularly spaced in Fig. 1, especially near the tipping points $WS \rightarrow HS$ and $WS \rightarrow CS$ where we have explored in detail the narrow region of stability of WS.

(Kucharski et al. 2013) in order to investigate how a different representation of a quantity linked to the transport of both energy and water mass affects the dynamics on the attractor (open blue circles in Fig. 1).

The energy, water, and entropy budgets in the multistable states are diagnosed with the help of TheDiaTo (Lembo et al. 2019). After running a simulation for over a thousand years until steady-state conditions are achieved on a given attractor, we continue it for 20 additional years saving daily and monthly averages of the fields in order to have sufficient statistics for employing the diagnostics. By estimating the energy and water budgets and the corresponding large-scale transports, the intensity of the Lorenz energy cycle (LEC) (Lorenz 1955; Peixoto and Oort 1992) and the material entropy production (MEP) (Peixoto and Oort 1992; Goody 2000; Pauluis and Held 2002; Lucarini 2009), TheDiaTo provides a synthetic and physically meaningful characterization of climate attractors. While details on the calculations of such diagnostics can be found in the original article (Lembo et al. 2019), the main equations are stated for completeness in the appendix, together with the interpolation and the steps needed to adapt MITgcm outputs for usage in TheDiaTo.

3. Characterization of the five aquaplanet climatic attractors

To quantify the relative importance of physical processes in multistable states, this section presents a detailed analysis of the five competing attractors obtained with $S_0 = 342 \text{ W m}^{-2}$ in SETUP-REF [as in Brunetti et al. (2019)]; see Fig. 1.

a. Energy and water-mass budgets and transports

Table 1 shows a selection of the average values of key global climatic observables for the five competing steady states. Average ocean temperatures range between $T = -1.9^\circ\text{C}$ for the SB climate and $T = 17.5^\circ\text{C}$ for the HS. Correspondingly, the mean surface air temperature (SAT) ranges between -38.75°C for the SB climate and 23.2°C for the HS (see Fig. S1 in the online supplemental material). Let us consider next the temperature difference between polar and equatorial regions (usually referred to as meridional temperature gradient), ΔT_{PE} . This is computed by taking the difference between the average surface air temperature in the latitudinal belt $30^\circ\text{S}\text{--}30^\circ\text{N}$ and in the region within 30° and 90° latitudes in the Northern and Southern Hemispheres (Lucarini and Bódai 2017; Margazoglou et al. 2021). One finds the smallest value ΔT_{PE} in the HS (16.2°C), which corresponds to conditions typical of so-called equitable climates (Huber and Caballero 2011). Instead, ΔT_{PE} is largest (34.3°C) for the CS.

The top-of-atmosphere (TOA) energy balance ranges between 0.3 and 2.9 W m^{-2} , which are typical values in coarse-resolution simulations such as those performed in phase 3 of the Coupled Model Intercomparison Project (CMIP3; <https://esgf-node.llnl.gov/projects/esgf-llnl/>) in the preindustrial scenario [see, e.g., Fig. 2a in Lucarini and Ragone (2011)]. The presence of an imbalance is in apparent contradiction with steady-state conditions; indeed, as discussed in Lucarini and Ragone (2011) and Liepert and Previdi (2012),

TABLE 1. Global mean values averaged over 20 years and associated standard deviation derived from interannual variability for the five attractors at $S_0 = 342 \text{ W m}^{-2}$ in SETUP-REF.

Description	Name	Units	HS	WS	CS	WB	SB
TOA budget	R_t	W m^{-2}	2.5 ± 0.2	2.5 ± 0.2	2.9 ± 0.1	1.7 ± 0.1	0.3 ± 0.1
Surface budget	F_s	W m^{-2}	0.2 ± 0.3	-0.0 ± 0.3	-0.1 ± 0.1	-0.1 ± 0.1	$(-2 \pm 6) \times 10^{-5}$
Ocean drift	$\partial T / \partial t$	$^{\circ}\text{C century}^{-1}$	0.05 ± 0.07	-0.01 ± 0.07	-0.02 ± 0.02	-0.02 ± 0.02	0 ± 0
Water budget	$E - P_{\text{tot}}$	$10^{-8} \text{ kg m}^{-2} \text{ s}^{-1}$	0 ± 2	0 ± 1	0 ± 1	4.3 ± 0.1	0.00 ± 0.03
Latent heat budget	R_L	W m^{-2}	0.01 ± 0.05	-0.01 ± 0.03	-0.01 ± 0.02	0.108 ± 0.004	-0.0001 ± 0.0007
Total precipitation	P_{tot}	$10^{-5} \text{ kg m}^{-2} \text{ s}^{-1}$	4.47 ± 0.02	4.08 ± 0.01	3.190 ± 0.008	0.435 ± 0.001	0.1043 ± 0.0005
Ocean temp	T	$^{\circ}\text{C}$	17.515 ± 0.001	9.990 ± 0.002	3.223 ± 0.002	-1.6401 ± 0.0005	-1.918127 ± 0.000003
Surface air temp	SAT	$^{\circ}\text{C}$	23.2 ± 0.2	17.0 ± 0.2	2.0 ± 0.1	-33.05 ± 0.03	-38.75 ± 0.04
Temp. gradient	ΔT_{PE}	$^{\circ}\text{C}$	16.2 ± 0.2	21.2 ± 0.2	34.3 ± 0.2	29.46 ± 0.08	21.5 ± 0.1
Mechanical work	W	W m^{-2}	2.43 ± 0.03	2.42 ± 0.04	2.06 ± 0.02	0.72 ± 0.02	0.37 ± 0.01

the spurious bias is due to physical processes that have been neglected, inconsistently treated, or approximated in climate models, as well as to unphysical effects of numerical dissipation (Pascale et al. 2011; Mauritsen et al. 2012; Lauritzen and Williamson 2019; Trenberth 2020). In our setting, the main contribution comes from the frictional heating (see section 4) and the fact that sea ice dynamics is neglected (Brunetti and V  rard 2018). Note that, as argued in Lucarini and Ragone (2011), the bias is positive in all cases.

The surface energy budget F_s ranges between -0.1 and 0.2 W m^{-2} for all climates. These values are in general smaller than those reported for CMIP3 control runs [see Fig. 4 in Lucarini and Ragone (2011)] or for CMIP5 control runs [see Table 2 in Lembo et al. (2019)]. The presence of such a small energy imbalance at the ocean's surface strongly indicates that all our simulations have reached a steady state (Brunetti and V  rard 2018), with a drift in the average oceanic temperature of only few parts in $10^{-2} \text{ }^{\circ}\text{C}$ per century (see Table 1). We remark that such accurate steady-state conditions were not imposed, but have been reached after a few thousand years of simulation, which were required to remove transient effects.

Table 1 also shows the global water budget, given by the difference between global averages of evaporation E and precipitation P_{tot} . We find that in all climates the bias in the water budget is negligible, so that approximately no water is lost during the numerical experiments, in agreement with Campin et al. (2008). This mirrors the presence of an accurately balanced latent heat budget R_L , also shown in Table 1, which is related to the phase transformation of water over different surfaces (see the appendix). For completeness, we also list the global annual mean precipitation P_{tot} , whose maximum value is found in HS.

In all climates, the atmospheric and the oceanic enthalpy³ transports (Fig. 2) are poleward and antisymmetric with respect to the equator as a result of the aquaplanet configuration, which is symmetric between the two hemispheres. The total transport balances the net TOA radiation influx in the

equatorial region and the net TOA outflux in the polar regions (Trenberth et al. 2009; Lucarini and Ragone 2011). Going from HS to CS, peaks of meridional enthalpy transport increase in magnitude (Fig. 2), mean surface air temperature decreases and meridional temperature gradient increases. The enthalpy transport is strongest in CS attractor with a peak of 6.5 PW in the atmosphere and 3.3 PW in the ocean. This is not surprising because the largest part of the atmospheric enthalpy transport in the extratropics is carried out by midlatitude eddies (Marshall and Plumb 2008, p. 155), in turn influenced by the meridional temperature gradient, while the oceanic heat transport is proportional to the strength of the circulation multiplied by the temperature gradient at the concerned latitudes (Boccaletti et al. 2005). Since CS has the steepest temperature gradient between pole and equator of the order of $\Delta T_{\text{PE}} = 34.3^{\circ}\text{C}$, it turns out that it also has the largest meridional enthalpy transport. Note that, despite the differences between HS, WS, and CS, their meridional atmospheric enthalpy transport peaks at the same latitude ($\sim 40^{\circ}\text{N/S}$) in agreement with the classical prediction by Stone (1978). The oceanic enthalpy transport is in all cases less intense than the atmospheric one and peaks at a lower latitude, as in the present-day Earth climate.

The much colder WB and SB climates are fundamentally different from the previous three in terms of transport profiles. In the WB climate, the atmospheric enthalpy transport peaks at the boundary of the water belt, where a large meridional temperature gradient is locally realized. Instead, the peak of the oceanic transport is obtained even closer to the equator and results from the intense overturning circulation inside the water belt. The meridional transports are negligible in the ice-covered portion of the planet. In the case of the SB climate, the oceanic transport vanishes due to the absence of an ice-free ocean surface, and the atmospheric transport is extremely weak at all latitudes, which, in turn, agree with the fact that 1) the meridional temperature differences are very small and 2) the atmosphere is dry (see Fig. 2c).

In the case of the three warmer climates, the annual mean meridional moisture transport (see Fig. 2c) is qualitatively similar to the present one, with the peak of the poleward transport occurring where the intensity of the meridional eddies is strongest—namely, in the storm track corresponding to the peak of the meridional enthalpy transport—whereas an

³ Following Lucarini and Ragone (2011) and Lembo et al. (2019), the enthalpy transport is given by $\mathbf{J}_h = \rho h \mathbf{v}$, where the standard definition of enthalpy $h = e + p/\rho$ is adopted, ρ being the density, e the total energy density of the fluid component, p the pressure, and \mathbf{v} the velocity vector.

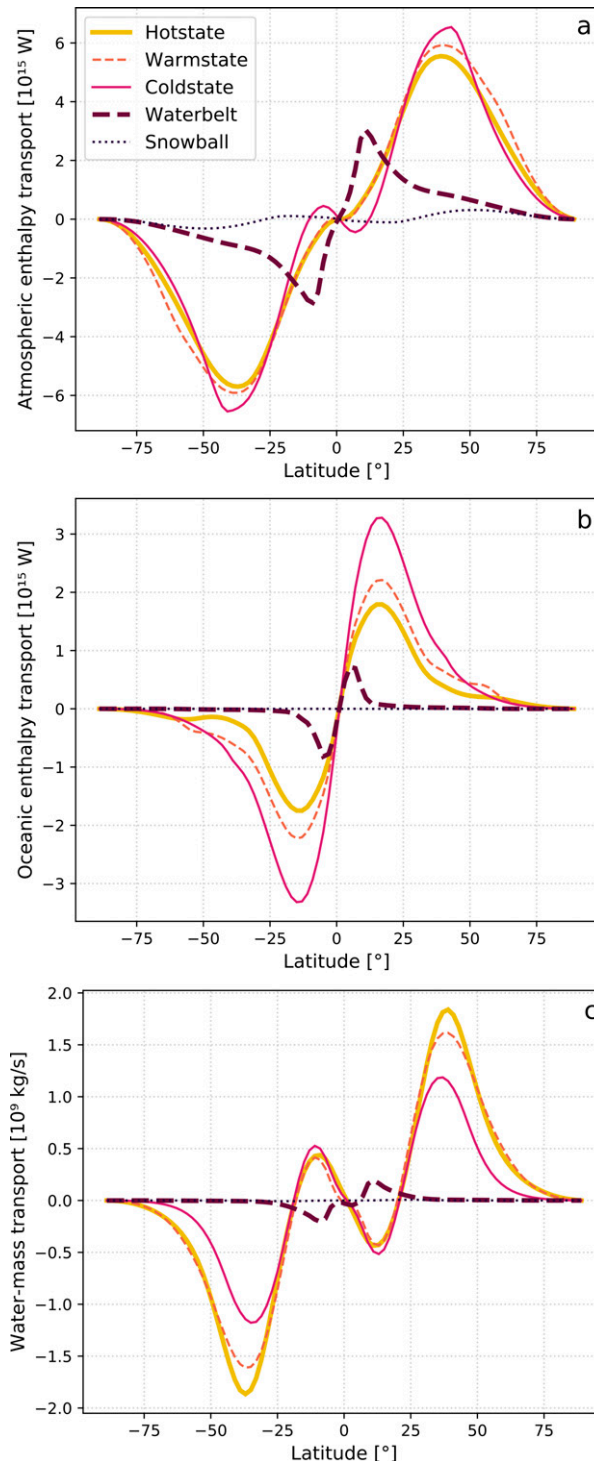


FIG. 2. Comparison of northward enthalpy transport in the (a) atmosphere and (b) ocean, and of (c) northward water mass transport in the five attractors of SETUP-REF for $S_0 = 342 \text{ W m}^{-2}$.

equatorward transport is realized in the tropical region, coincident with the Hadley cells. Note that the largest poleward transport is obtained in the HS climate because higher surface temperature favors evaporation. Considering that the HS

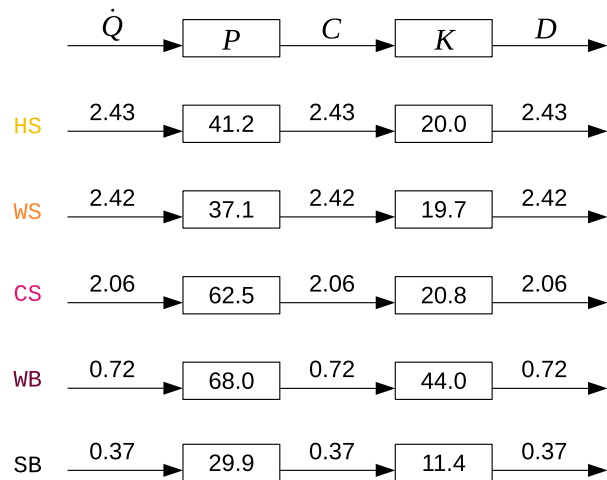


FIG. 3. Simplified Lorenz energy cycle for the five attractors in SETUP-REF for $S_0 = 342 \text{ W m}^{-2}$. Storage terms (boxes) of available potential energy P and kinetic energy K are in 10^{15} J m^{-2} ; generation \dot{Q} , conversion C , and dissipation D terms (arrows) are in W m^{-2} . Standard deviations, derived from interannual variability and associated with each value from HS to SB, are $(0.03, 0.04, 0.02, 0.02, 0.01) \text{ W m}^{-2}$ for \dot{Q} , C , and D ; $(0.8, 0.5, 0.9, 0.5, 0.4) \times 10^{15} \text{ J m}^{-2}$ for P ; and $(0.2, 0.2, 0.1, 0.4, 0.5) \times 10^{15} \text{ J m}^{-2}$ for K .

has the weakest total enthalpy transport (Fig. 2a), one deduces that large-scale latent heat transport is relatively more important in the HS. Clearly, meridional moisture transport is almost vanishing in the SB climate, because evaporative processes are virtually absent, and is very weak and concentrated over and near the water belt in the WB climate.

b. Lorenz energy cycle

The Lorenz energy cycle (LEC) describes the time-averaged transformation of energy between the available potential form and the kinetic form. The reservoir of available potential energy P is continuously replenished thanks to the inhomogeneous absorption of radiation, while the kinetic energy K is continuously depleted as a result of dissipative processes (Lorenz 1955). This is the starting point for treating the atmosphere as a nonideal engine, for defining its efficiency, and evaluating its entropy production (Peixoto and Oort 1992; Goody 2000; Pauluis and Held 2002; Lucarini 2009).

Specifically, a simplified version⁴ of the LEC can be represented in terms of two energy reservoirs and three conversion terms as in Pascale et al. (2011), where the available potential energy reservoir P evolves due to generation by diabatic heating \dot{Q} and conversion of potential to kinetic energy C . On the other hand, the kinetic energy reservoir K is affected by the

⁴ The more general version of LEC is able to distinguish between processes occurring at different scales of motion and to describe energy exchanges across scales (Lorenz 1955; Peixoto and Oort 1992); see the online supplemental material.

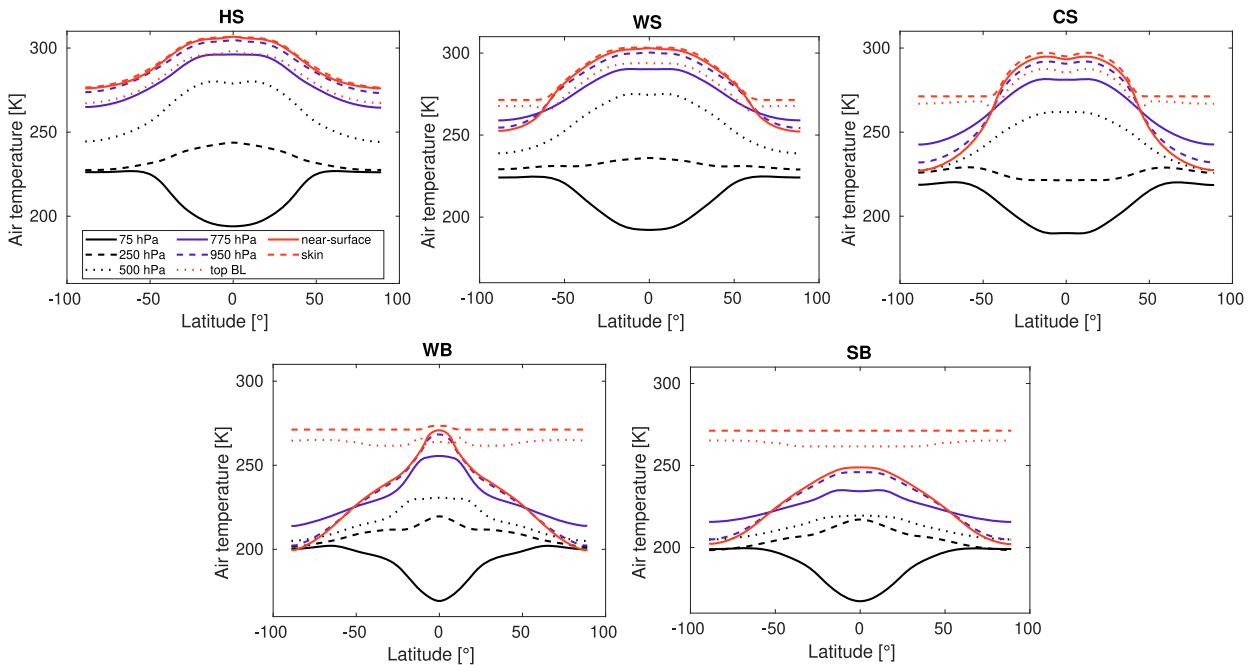


FIG. 4. Zonal average of air temperature at different pressure levels in the five attractors in SETUP-REF for $S_0 = 342 \text{ W m}^{-2}$.

conversion term C and the dissipation term D . For sake of clarity, the LEC can be formally summarized by the following budget equations:

$$\dot{P} = -C(P, K) + \dot{Q}, \quad (1)$$

$$\dot{K} = -D + C(P, K). \quad (2)$$

The definitions of reservoir and conversion terms are given in the online supplemental material and in Lembo et al. (2019).

As shown in Fig. 3, the reservoir of available potential energy P is smaller in HS and WS than in CS, in agreement with the fact that, as far as simulations of the actual Earth are concerned, it decreases from preindustrial to present-day conditions (Lembo et al. 2019). Note that P is proportional to the variance of temperature on isobaric surfaces in the free troposphere, and to the inverse of the difference in the lapse rate of dry versus moist air, $\Gamma_d - \Gamma$ [Lorenz 1955, see Eq. (10) therein]. The former is dominated by the variance with respect to the zonal mean (see the online supplemental material), in turn related to meridional temperature gradients in the free atmosphere (Fig. 4), while $\Gamma_d - \Gamma$ is larger in warmer conditions (Marshall and Plumb 2008, p. 49). The combined effect of such contributions can explain the values of P in the attractors. The fact, for example, that P in HS is larger than in WS depends on weaker meridional gradients in WS at 250, 500, and 775 hPa, as shown in Fig. 4. On the other hand, the reservoirs of kinetic energy K , depending on the variance of wind speed, are very similar for HS, WS, and CS (Fig. 5). Consequently, the sum of kinetic and available potential energy is different between the attractors.

The WB climate features the largest reservoirs of both available potential and kinetic energy. Indeed, the presence of a

very intense temperature gradient localized at the ice edge (Fig. 4) and governing the dynamics (Brunetti et al. 2019) leads to large values of the available potential energy and allows for the presence of very intense zonal winds at low latitudes and at intermediate pressure levels, as shown in Fig. 5. In this attractor, jet streams are so intense that the mean kinetic energy reservoir amounts to almost 0.65 times the mean potential energy reservoir. The SB climate, instead, features the smallest reservoirs for both forms of energy as a result of the weak temperature gradients and weak atmospheric circulations throughout the domain.

Statistically steady-state conditions imply that the long-term time-average values of the diabatic heating \dot{Q} , of the conversion term C (which can also be seen as the mechanical work W performed by the climatic engine or as the intensity of the LEC), and of the dissipation D are identical. This is indeed the case for the values obtained for the five competing climatic attractors (Fig. 3 and Table 1). The intensity of the LEC is found to be considerably higher for the three warmer climates, where it ranges between 2.06 and 2.43 W m^{-2} . These figures are in broad agreement with the values obtained with seven climate models participating in CMIP5 using preindustrial conditions (see Table 2 in Lembo et al. 2019), as well as with those found in additional CMIP5 model runs and in reanalysis datasets (Veiga and Ambrizzi 2013; Li et al. 2007). In contrast to the warmer climates, the intensity of the LEC is much weaker in the WB and in the SB climates, where weather variability is greatly reduced and localized in a narrow band (WB) or virtually absent (SB); see Lucarini et al. (2010) for a detailed analysis of the thermodynamics of the SB state. Note that, as well known (Lorenz 1955), there is no obvious relationship between the size of the energy reservoirs

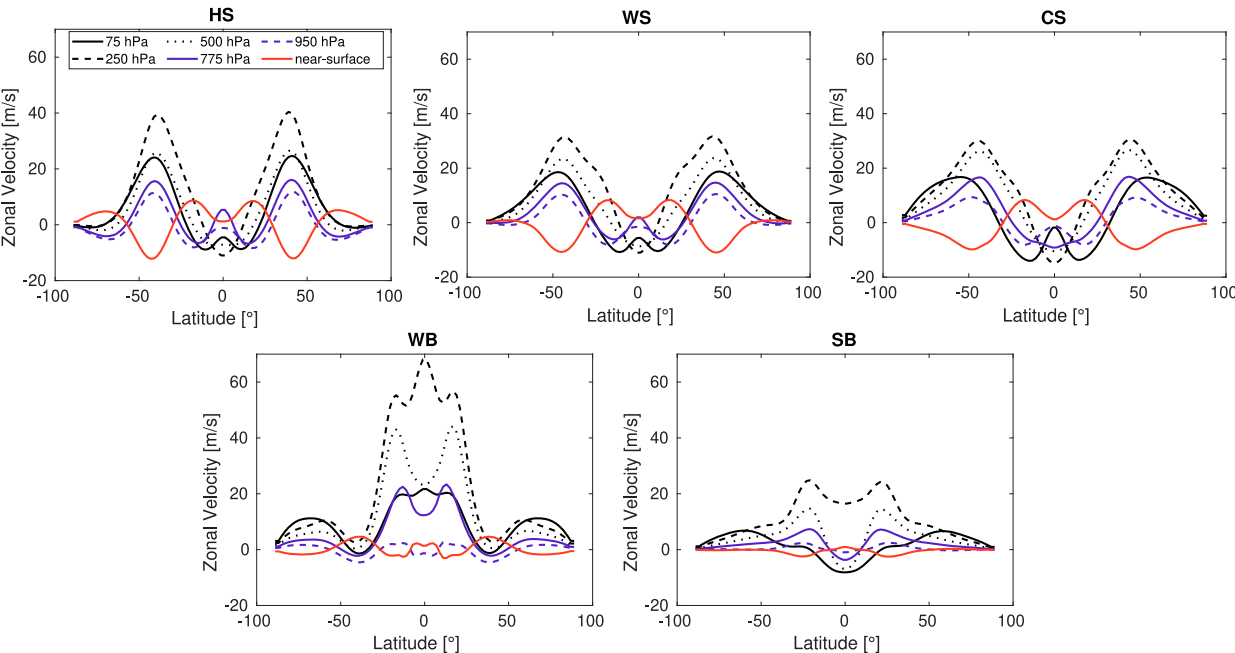


FIG. 5. Zonal wind at different pressure levels in the five attractors in SETUP-REF for $S_0 = 342 \text{ W m}^{-2}$.

and the value of the conversion terms, so the fact that the WB state has the largest reservoirs of energy is not in contradiction with the very low intensity of the LEC.

c. Material entropy production

In the Earth system energy undergoes transport and transformation processes, and entropy is continuously produced by irreversible mechanisms. At steady state, while a zero net energy flux is reached at the boundary of the system, the entropy production is balanced by a net outgoing flux of entropy toward space. The entropy production can be partitioned into two main components (Lucarini et al. 2014; Bannon 2015). One—the dominant part—describes the irreversible transformation of the radiation from short wave to infrared. The second part, usually referred to as material entropy production (MEP), is generated by fluid motions mainly through 1) dissipation of kinetic energy due to viscous processes, 2) irreversible processes associated with moisture, and 3) sensible heat fluxes at the interface between the atmosphere and the surface (Peixoto and Oort 1992; Goody 2000;

Pauluis and Held 2002; Pauluis 2007; Lucarini et al. 2011). In the current climate, term 3 in the list above (sensible heat fluxes) is the smallest, followed by term 1, whereas irreversible moist processes give by far the most relevant contribution to the total MEP (Goody 2000; Pascale et al. 2011; Lucarini and Pascale 2014). Moist processes are embedded in the hydrological cycle, namely the phase changes (e.g., evaporation, condensation, and sublimation taking place in nonsaturated environment), and the dissipation of kinetic energy from precipitating hydrometeors [see Eq. (A5)].

For sake of simplicity, TheDiaTo neglects the phase changes occurring within the clouds during the formation and depletion of rain/snow droplets. Moreover, it deliberately focuses on MEP related to irreversible processes in the atmosphere, as it was previously shown (Pascale et al. 2011) that the contribution of the ocean to the MEP budget is at least one order of magnitude smaller than the atmospheric contribution.

Table 2 lists individual contributions to MEP for the five attractors. The total MEP increases with the mean surface air

TABLE 2. Contributions to material entropy production (MEP; $\text{mW m}^{-2} \text{ K}^{-1}$) in the five attractors at $S_0 = 342 \text{ W m}^{-2}$ in SETUP-REF.

MEP associated with...	Hot state	Warm state	Cold state	Waterbelt	Snowball
Viscous processes	8.3 ± 0.1	8.4 ± 0.1	7.32 ± 0.08	2.70 ± 0.06	1.39 ± 0.04
Hydrological cycle	47 ± 4	42 ± 2	30 ± 1	2.7 ± 0.2	0.89 ± 0.09
Evaporation	-371 ± 2	-342 ± 1	-272.0 ± 0.6	-40.3 ± 0.1	-9.62 ± 0.04
Potential energy of droplets	6.30 ± 0.05	5.50 ± 0.03	3.77 ± 0.01	0.386 ± 0.001	0.1194 ± 0.0004
Precipitation	412 ± 2	379 ± 1	298.7 ± 0.7	42.6 ± 0.1	10.39 ± 0.05
Sensible heat diffusion	1.07 ± 0.03	1.55 ± 0.02	2.409 ± 0.007	2.558 ± 0.007	2.547 ± 0.006
Total MEP	56 ± 4	52 ± 2	40 ± 1	8.0 ± 0.3	4.8 ± 0.1

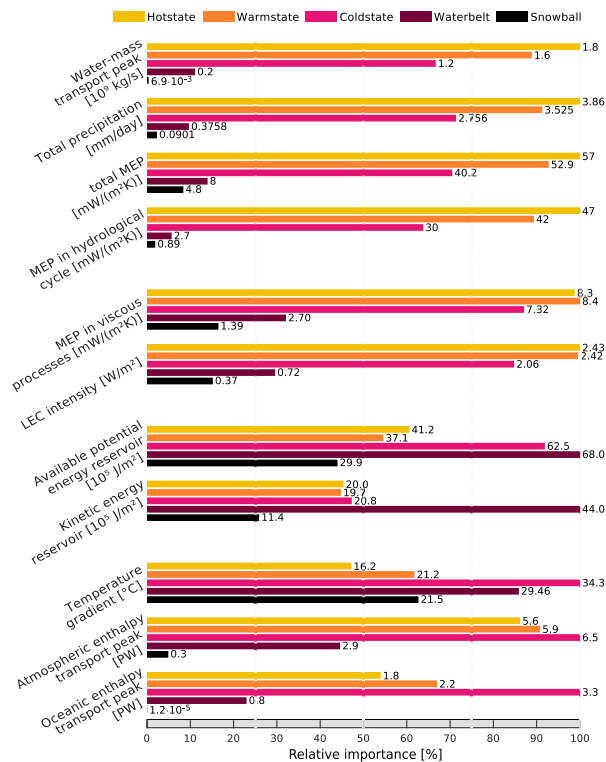


FIG. 6. Summary of the main climatic variables and of their values in the five states in SETUP-REF for $S_0 = 342 \text{ W m}^{-2}$. The relative value is expressed with respect to the largest one realized among the five states.

temperature (i.e., from SB to HS) (Lucarini et al. 2010) mainly because the hydrological cycle is stronger in a warmer environment (Held and Soden 2006; see also Fig. 2c herein). In contrast, the contribution coming from the diffusion of sensible heat is larger in colder climates, albeit it only represents a small fraction of the total MEP. This quantity depends on the product of the sensible heat flux, H_S , and the difference between top-of-boundary layer and skin temperatures, $T_{\text{BL}} - T_s$ [see second term in Eq. (A5)]. As can be seen in Fig. 4, it turns out that while $T_{\text{BL}} - T_s$ is of the same order in all attractors, the sensible heat flux H_S is larger in colder climates, since it depends on the difference between skin and near-surface temperatures (Marshall and Plumb 2008, p. 226).

d. Summary

The analysis performed so far is summarized in Fig. 6, where for each considered climatic variable the relative value is expressed with respect to the largest one realized among the five states. This visually highlights how, under the same forcing, the processes balance in a different way in coexisting attractors. It also helps in understanding how different variables are connected between each other, and which are the key quantities that identify a climatic state. In particular, we see that MEP due to the hydrological cycle (which represents the largest contribution to total MEP) is linked to total precipitation and the peak intensity in the water-mass transport. These

quantities, together with the global temperature, are maximized in the HS, an ice-free steady state. On the other hand, the LEC intensity is closely linked to MEP due to viscous processes, which is largest in the WS. The meridional temperature gradient influences the enthalpy transport in both the ocean and the atmosphere, showing the most prominent peaks in the CS. Localized gradients of temperature and wind speed in the free troposphere increase the variance of such quantities, thus maximizing values of P and K , respectively, as in WB. Finally, SB minimizes all the above quantities. The inclusion of LEC and MEP is crucial to distinguish the behavior of WB and WS from the other steady states, thus showing the relevance of using TheDiaTo for attractors characterization.

4. Effect of removing the energy bias by the reinjection of the dissipated kinetic energy

After having characterized the attractors, we can now evaluate their robustness against different model configurations. Kinetic energy within eddies is dissipated at small scales through an energy cascade (i.e., the dissipation term denoted as DE in the complete LEC; see the supplemental material). Energy conservation imposes that such dissipated mechanical energy should enter again into the energy budget as it is eventually converted into internal energy by friction. This term is usually ignored in general circulation models, as it is much smaller than other contributions, such as the latent heat exchanges. However, one should keep in mind that the frictional dissipation is positive definite, and, hence, does play a role in the overall energy budget. It has been shown that neglecting this term gives rise to a spurious thermal forcing of up to 2 W m^{-2} (Becker 2003) and could explain part of the bias observed in TOA energy imbalance for the climate models (Lucarini and Ragone 2011; Wild 2020). Thus, we have performed a sensitivity experiment, in which we evaluate the impact of the reinjection of dissipated kinetic energy on the modeled energy budget and the other thermodynamic diagnostics computed in TheDiaTo. To assess the relevance of this effect, we focus on the HS, comparing the standard setup SETUP-REF and the energy-consistent setup SETUP-FH for $S_0 = 342 \text{ W m}^{-2}$; see Fig. 1.

While the imbalances of water mass and surface energy are similar in both cases, as shown in Table 3, the TOA imbalance is almost exactly reduced to zero (within the confidence interval) when frictional heating is reinjected as in SETUP-FH, confirming the importance of including such term in climate simulations. This improved conservation of energy gives rise to an increase of mean surface air temperature of 1.72°C (see Table 3) and an average increase of 1.4°C in the five atmospheric layers, as conjectured in Lucarini and Ragone (2011).

The transport of enthalpy is slightly less intense in SETUP-FH, as shown in Figs. 7a and 7b. The energy reinjection is local in space and time and takes place mostly in the midlatitudes, which is where the strongest dissipation occurs. Hence, heat is added in a region where the annual-mean TOA budget is negative (see Fig. S3). As a result, the peak value of the meridional enthalpy transport as well as the meridional temperature gradient ΔT_{PE} decrease in SETUP-FH, as shown in

TABLE 3. Comparison of hot states at 342 W m^{-2} in SETUP-REF and SETUP-FH. Statistically different values are in boldface.

Description	Name	Units	SETUP-REF	SETUP-FH
Surface air temperature	SAT	$^{\circ}\text{C}$	23.2 ± 0.2	24.92 ± 0.08
Meridional temperature gradient	ΔT_{PE}	$^{\circ}\text{C}$	16.2 ± 0.2	15.44 ± 0.09
TOA energy budget	R_t	W m^{-2}	2.5 ± 0.2	0.0 ± 0.2
Surface energy budget	F_s	W m^{-2}	0.2 ± 0.3	0.2 ± 0.2
Water budget	$E - P_{\text{tot}}$	$10^{-8} \text{ kg m}^{-2} \text{ s}^{-1}$	0 ± 2	0 ± 2
Total precipitation	P_{tot}	$10^{-5} \text{ kg m}^{-2} \text{ s}^{-1}$	4.47 ± 0.02	4.56 ± 0.02
Mechanical work	W	W m^{-2}	2.43 ± 0.03	2.33 ± 0.03

Figs. 7a and 7b and in Table 3, respectively. Instead, the local increase in the surface temperature leads, as a result of enhancement of evaporation, to a slight strengthening of the meridional moisture transport in SETUP-FH with respect to the reference setup SETUP-REF (Fig. 7c).

The LEC for the two setups are compared in Fig. 8. Dissipation D is 4% smaller in SETUP-FH than in the reference setup. In a steady state, the generation of available potential energy \dot{Q} and the dissipation D have to balance and hence \dot{Q} has to decrease by an equal amount. This is consistent with a weaker meridional enthalpy transport in the atmosphere, as observed in Fig. 7a, and with a smaller meridional temperature gradient (from equator to poles; see Table 3).

While the intensity of the atmospheric circulation is lower in SETUP-FH, as measured by the mechanical work $W \sim D$, its hydrological cycle becomes slightly more effective, as already observed for the water-mass transport in Fig. 7c, with statistically significant larger values of material entropy production associated with precipitation and condensation, as shown in Table 4. Heating the lower levels of the atmosphere strengthens the hydrological cycle and favors vertical transport of water vapor. Overall, the total MEP remains approximately constant because the slightly strengthening of the hydrological cycle in SETUP-FH is compensated by the reduced contribution of viscous processes and sensible heat diffusion.

In summary, reinjecting frictional heating improves the TOA budget, as expected, but has also several additional consequences that have been revealed by TheDiaTo: on the one hand, the increased mean temperature of the atmospheric column, particularly over the midlatitudes, has strengthened the total precipitation and MEP associated to it; on the other hand, the reduced dissipation of energy has weakened the mechanical work of the LEC and the diabatic heating related to the meridional temperature gradient, and consequently the meridional enthalpy transport.

5. Testing different cloud albedo representations

A new representation for the cloud albedo has been introduced in the latest version of the atmospheric module SPEEDY (called ICTPAGCM; Kucharski et al. 2006, 2013) in order to reduce the net solar radiation at high latitudes and, hence, to have better agreement with observational data. The cloud albedo is assumed to depend on the latitude ϕ :

$$\alpha_C(\phi) = \begin{cases} \alpha_{C0} + 0.2|\sin(\phi)|^4 & \text{if } \cos(\phi) > \frac{1}{2} \\ \alpha_{C0} + 0.2|\sin[\arccos(1/2)]|^4 & \text{elsewhere,} \end{cases} \quad (3)$$

so that $\alpha_C(\phi)$ increases poleward from a value of $\alpha_{C0} = 0.38$ at the equator up to a maximum value of ≈ 0.4925 at 60°S/N , and then holds constant up to the poles.

The physical rationale behind such a representation is that cloud cover appears effectively thicker when radiation is coming from lower geometrical angles. We have thus included such a modification in the atmospheric module of MITgcm and we call this configuration SETUP-FH-CL.

If we consider an incoming solar radiation of 342 W m^{-2} , the WB and SB states are observed in both SETUP-FH and SETUP-FH-CL (see Fig. 1). We will not investigate the effect of changing the cloud albedo representation for these two climates because they feature very weak dynamical processes and because they are in deep frozen state with high-albedo surface at high latitudes, so that the effect of changing the albedo of high-latitude clouds can be understood as minimal.

To compare the effects of the cloud albedo prescription on attractors with stronger mechanical work, we consider an incoming solar radiation of 341 W m^{-2} and look at the cold climates realized with SETUP-FH and SETUP-FH-CL; see the red diamonds and blue circles in Fig. 1.⁵

Table 5 gives the key output characterizing the attractor in both configurations. First of all, it is important to verify that the new representation affects neither the global water-mass budget nor the energy budget. The increase of cloud albedo at high latitudes reduces the amount of incoming radiation, and the mean surface air temperature by nearly 6°C . This is correlated to a larger sea ice extent in SETUP-FH-CL. However, both values of the sea ice cover are of the same order ($120\text{--}160$ million km^2) as those found in the cold climates at $S_0 = 342 \text{ W m}^{-2}$ [see Table 2 in Brunetti et al. (2019)], suggesting that both attractors are of the same type. As a result of the more uneven absorption of solar radiation between high and low latitudes, the transports of enthalpy in both the atmosphere and the ocean (Figs. 9a,b) are stronger in SETUP-FH-CL. Moreover, the larger sea ice extent

⁵ Note that for this value of the incoming solar radiation the HS becomes unstable in SETUP-FH and morphs into a climate that is close to the CS in SETUP-FH-CL.

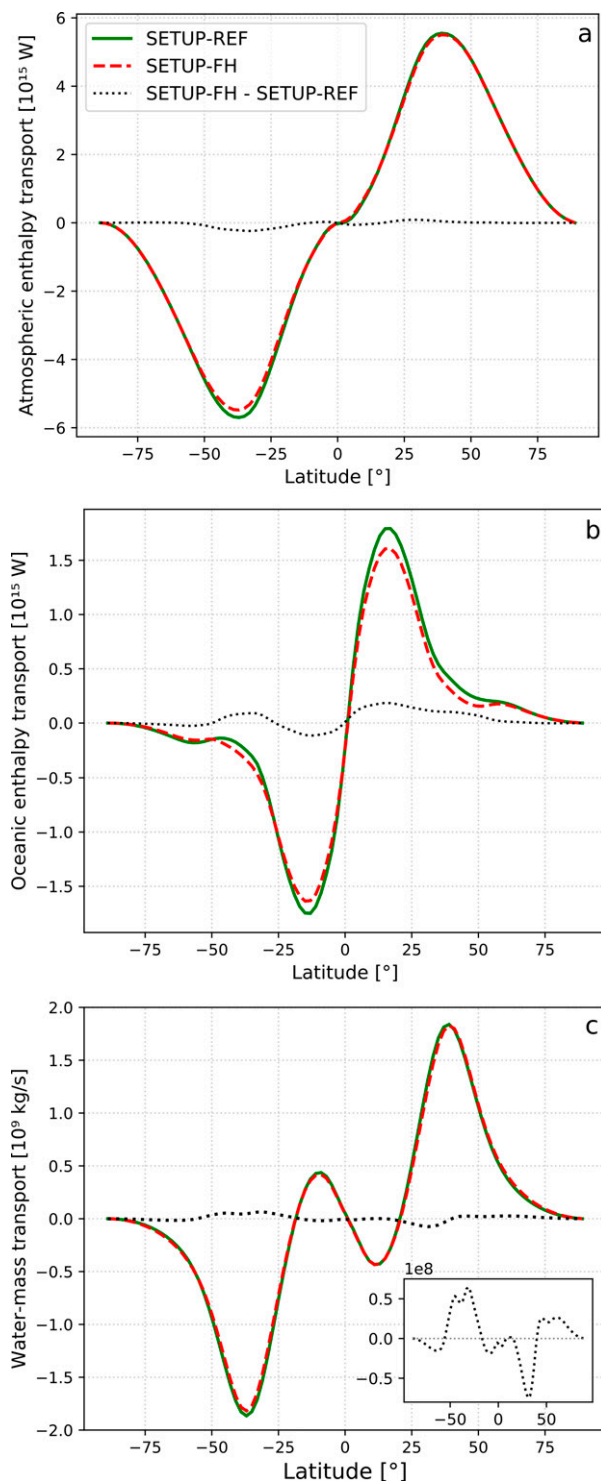


FIG. 7. Comparison of hot states at $S_0 = 342 \text{ W m}^{-2}$ in SETUP-REF and SETUP-FH in terms of northward enthalpy transport in the (a) atmosphere and (b) ocean, and of (c) water-mass transport, where the inset is a zoom of the difference.

determines an equatorward displacement of the peaks in the atmospheric transport. Consistently with what was found in section 3, the SETUP-FH-CL climate has a higher

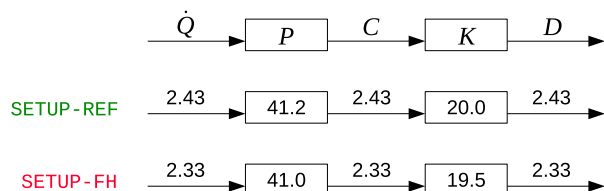


FIG. 8. Simplified Lorenz energy cycle for hot states at $S_0 = 342 \text{ W m}^{-2}$ in SETUP-REF and SETUP-FH. Storage terms (boxes) in 10^5 J m^{-2} and conversion terms (arrows) in W m^{-2} . Standard deviations are 0.03 W m^{-2} for \dot{Q} , C , and D ; $0.8 \times 10^5 \text{ J m}^{-2}$ for P ; and $0.2 \times 10^5 \text{ J m}^{-2}$ for K , in both setups.

reservoir of available potential energy P (see Fig. 10) and a weaker moisture transport with its main peaks located closer to the equator, as shown in Fig. 9c. Indeed, the average temperature of the planet is greatly reduced with the new high-latitude cloud albedo prescription, hence the atmosphere as a whole becomes much drier, and a larger sea ice extent reduces the ocean surface available for water evaporation.

The total MEP turns out to be significantly lower in SETUP-FH-CL, as a result of a smaller contribution in all components of the MEP budget, except for MEP associated with sensible heat diffusion and viscous processes, as shown in Table 6. This is due to the weaker hydrological cycle in SETUP-FH-CL, confirming the trend observed in section 3 for attractors with colder temperatures. The change in MEP associated with viscous processes is not statistically significant, and the same holds for the intensity of LEC that is comparable in the two setups, of the same order as in CS at $S_0 = 342 \text{ W m}^{-2}$ in SETUP-REF or SETUP-FH-CL, and lower than in WS (see Table 5 and Fig. 10), showing that the attractor is robust with respect to the new cloud prescription.

All in all, when looking at the CS, including the new representation leads to a decrease in the total MEP by $\sim 11.4\%$ due to a weaker hydrological cycle, and strengthens the enthalpy transport in both the atmosphere and the ocean, without introducing any spurious bias in water and energy budgets. Since Kucharski et al. (2006) showed that such cloud albedo prescription improves comparisons with observational data in present-day simulations, we can conclude that it is worth including it in the MITgcm atmospheric module.

TABLE 4. Contributions to MEP ($\text{mW m}^{-2} \text{ K}^{-1}$) in hot states with SETUP-REF and SETUP-FH at 342 W m^{-2} . Statistically different values are in boldface.

MEP associated with...	SETUP-REF	SETUP-FH
Viscous processes	8.3 ± 0.1	7.9 ± 0.1
Hydrological cycle	47 ± 4	48 ± 3
Evaporation	-371 ± 2	-377 ± 1
Potential energy of droplets	6.30 ± 0.05	6.53 ± 0.03
Precipitation	412 ± 2	419 ± 2
Sensible heat diffusion	1.07 ± 0.03	0.91 ± 0.02
Total MEP	56 ± 4	57 ± 3

TABLE 5. Comparison of cold states at 341 W m^{-2} in SETUP-FH and SETUP-FH-CL. Statistically different values are in boldface.

Description	Name	Units	SETUP-FH	SETUP-FH-CL
Surface air temperature	SAT	$^{\circ}\text{C}$	8.93 ± 0.08	2.67 ± 0.09
Meridional temperature gradient	ΔT_{PE}	$^{\circ}\text{C}$	27.3 ± 0.2	33.5 ± 0.2
Sea ice extent	—	10^6 km^2	118.7 ± 0.8	159 ± 1
TOA energy budget	R_t	W m^{-2}	-0.3 ± 0.2	-0.3 ± 0.2
Surface energy budget	F_s	W m^{-2}	0.0 ± 0.2	0.0 ± 0.2
Water budget	$E - P_{\text{tot}}$	$10^{-9} \text{ kg m}^{-2} \text{ s}^{-1}$	-5 ± 8	-5 ± 8
Total precipitation	P_{tot}	$10^{-5} \text{ kg m}^{-2} \text{ s}^{-1}$	3.537 ± 0.009	3.168 ± 0.009
Mechanical work	W	W m^{-2}	1.98 ± 0.03	2.02 ± 0.02

6. Summary and conclusions

The climate is a nonequilibrium, multiscale system that features multistability. The occurrence of such a phenomenon arises from its complex dynamics where forcing, dissipative processes, and nonlinear feedbacks can balance each other in different ways. The presence of multistability is intimately connected to the existence of tipping points coming with qualitative changes in the system dynamics for suitably defined forcings. In a deterministic setting, multistability is described by the presence of more than one competing steady state associated with different attractors, each included in a separate basin of attraction. While the dynamics of an autonomous system is confined to a single attractor, as its evolution is uniquely defined by its initial condition, the presence of stochastic forcings makes it possible for the system to explore the full phase space by performing transitions between the various basins of attraction (Benzi et al. 1983; Saltzman 2001; Lucarini and Bóday 2019; Lucarini and Bóday 2020; Ghil and Lucarini 2020).

We performed simulations using the MIT general circulation model with coupled aquaplanet configuration and different values of the incoming solar radiation S_0 in order to construct the bifurcation diagram (Fig. 1). Such methodology and the resulting graph are crucial to identify multistable regions, tipping points, and the range of stability of each attractor. The model displays five attractors that coexist for solar constant values in the range $1368\text{--}1370 \text{ W m}^{-2}$ (see Fig. 1): the classical “snowball” (SB) and “warm state” (WS) solutions; the very cold waterbelt (WB) state, where a water belt is present near the equator; the “cold state” (CS), where sea ice extends to the midlatitudes; and the “hot state” (HS), an equitable climate where no sea ice is present at all.

To describe the properties of such competing climatic states, we made use of a newly developed diagnostics tool, TheDiaTo (Lembo et al. 2019), that is part of the most recent version of the ESMValTool suite for evaluating Earth system models (Eyring et al. 2020). TheDiaTo provides flexible tools for the characterization of fundamental thermodynamic and conservation laws, starting from first principles. More specifically, we have focused on global averages and patterns of near-surface temperatures, water mass, and TOA and surface energy budgets, hence describing the strength of the meridional enthalpy and moisture transports, as well as the atmospheric Lorenz energy cycle (LEC) through its reservoirs, sources, sinks, and conversion terms. The second law of

thermodynamics has been assessed through the retrieval of material entropy production (MEP)—that is, the entropy change related to irreversible processes, such as the energy exchanges through sensible heat fluxes and the hydrological cycle. We have found the key processes that characterize each attractor: total precipitation, peak intensity in water-mass transport, and global temperature are maximized in HS; LEC intensity and MEP in viscous processes are large in WS; meridional temperature gradient and enthalpy transport are dominant in CS; P and K are maximized when localized gradients of temperature and wind speed are present, as in WB; SB minimizes all the previous quantities. These findings provide hints for using different climatic variables on reduced phase space for each climatic state, a subject that we will explore in further studies.

Exploring the multistability of the climate system requires us to consider a wide range of initial conditions and detailed characterization of the resulting climates. Such framework is of great relevance for modeling paleoclimate conditions (Pohl et al. 2014; Brunetti et al. 2015; Ferreira et al. 2018; Messori and Faranda 2020), where large uncertainty exists in initial conditions, as well as for the study of exoplanets, where the probability of finding an habitable planet is increased when multistability is allowed (Seager 2013; Boschi et al. 2013). Characterizing the basic properties of the modeled dynamics and thermodynamics is thus crucial in order to suitably represent the tipping points of the climate system (Lenton et al. 2008) and allow for a more general definition of climate sensitivity (von der Heydt and Ashwin 2017; Ashwin and von der Heydt 2020).

The complete set of metrics in TheDiaTo can be used not only to quantitatively differentiate the attractors but also to highlight biases due to a simplified representation of physical processes in climate models. For testing this last point, we performed two numerical experiments. First, focusing on the HS, we forced reinjection of frictionally dissipated kinetic energy into the overall energy budget. On one hand, such correction effectively leads to a reduction in the TOA energy bias, as expected. On the other hand, it influences the dynamics of the atmosphere in a nontrivial way, as the reinjection is collocated with the frictional dissipation. The climate becomes warmer and the meridional temperature gradient is reduced, as well as the LEC intensity, while the total precipitation and MEP associated with it increase. Second, focusing on the CS, we investigated the effect of introducing a dependency on latitude in the cloud albedo (cf. Kucharski et al. 2006, 2013). The

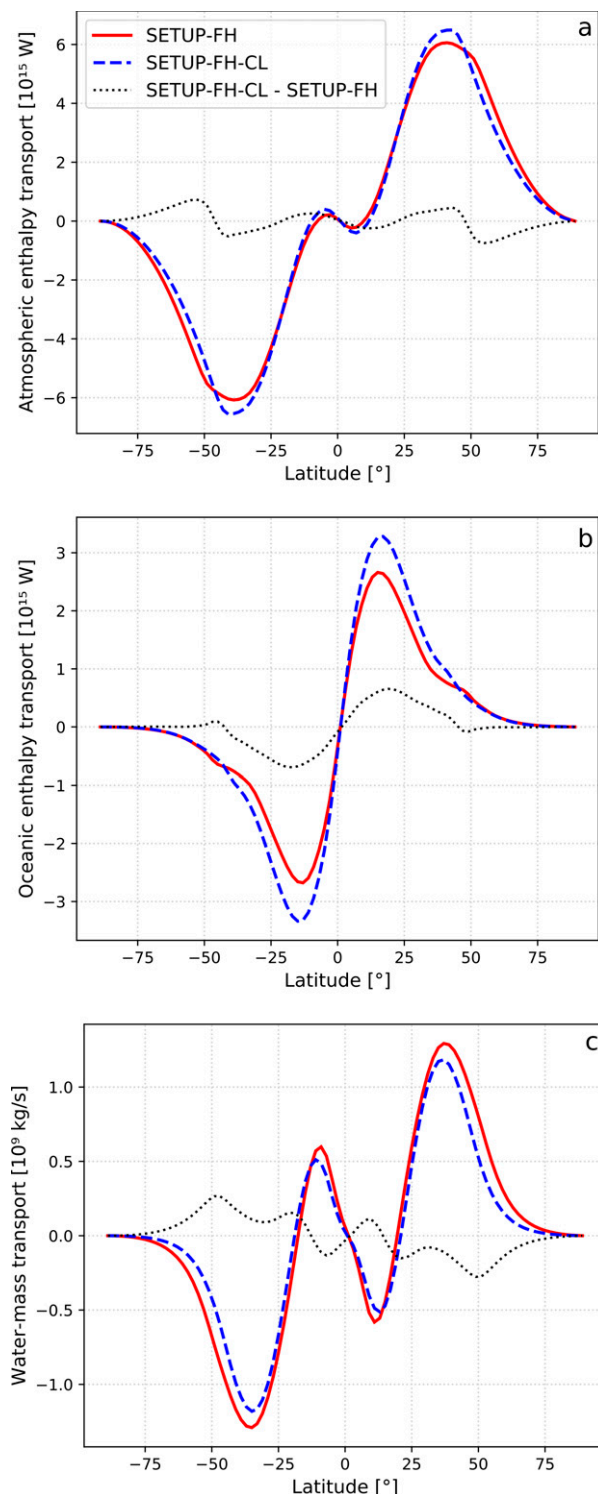


FIG. 9. Comparison of cold states at $S_0 = 341 \text{ W m}^{-2}$ in SETUP-FH and SETUP-FH-CL in terms of enthalpy transport in the (a) atmosphere and (b) ocean, and of (c) water-mass transport.

implementation of such a scheme does not affect global conservation properties but does cause changes in energy and moisture fluxes that lead to a cooler climate, with a weaker

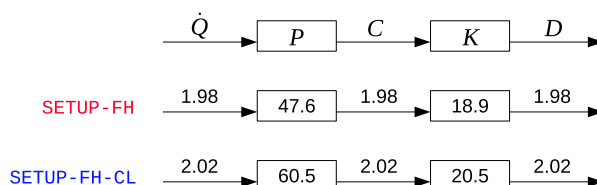


FIG. 10. Simplified Lorenz energy cycle for cold states at 341 W m^{-2} in SETUP-FH and SETUP-FH-CL. Storage terms (boxes) in 10^5 J m^{-2} and conversion terms (arrows) in W m^{-2} . Standard deviations are 0.03 and 0.02 W m^{-2} for \dot{Q} , C , and D ; 0.8 and $0.8 \times 10^5 \text{ J m}^{-2}$ for P ; and 0.2 and $0.1 \times 10^5 \text{ J m}^{-2}$ for K , in SETUP-FH and SETUP-FH-CL, respectively.

hydrological cycle and MEP. Despite these changes, TheDiaTo allowed us to verify that the attractors are of the same type (CS), showing that useful information can be inferred as to the attractor's nature even without the construction of the complete bifurcation diagram.

In summary, in both the numerical experiments the set of metrics in TheDiaTo has clearly shown that the climate state slightly changes, remaining on the same attractor, with nonnegligible impacts on the dynamics and thermodynamics, while at the same time preserving or improving the global conservation properties. Thus, TheDiaTo helps in controlling simulation quality and in evaluating different configurations. In particular, LEC and MEP, two metrics that are not routinely used for model evaluation, can provide additional benchmarks when constrained by observational data in present-day climate simulations.

While TOA energy imbalance can be improved though the inclusion of missing physical processes (such as frictional heating) or enhanced algorithms (with less numerical dissipation, for example), the energy imbalance at the surface F_s is less affected by such procedures. As shown in several previous diagnostic studies, the *ghost* energy bias is concentrated in the atmosphere (Lucarini and Ragone 2011; Lucarini et al. 2014; Lembo et al. 2017). Instead, F_s stabilizes as one considers longer simulation time, which allows the ocean to reach an approximate steady state. A vanishing surface energy imbalance (as assured in our simulations) guarantees that the drift of the mean ocean temperature is negligible. Thus, TOA and surface energy imbalance should be always monitored in climate models (Brunetti and V  rard 2018) and we encourage researchers to explicitly list them when presenting simulation results.

TABLE 6. Contributions to MEP ($\text{mW m}^{-2} \text{ K}^{-1}$) in cold states with SETUP-FH and SETUP-FH-CL at 341 W m^{-2} . Statistically different values are in boldface.

MEP associated with...	SETUP-FH	SETUP-FH-CL
Viscous processes	7.0 ± 0.1	7.18 ± 0.09
Hydrological cycle	35 ± 2	30 ± 2
Evaporation	-299.4 ± 0.7	-270.0 ± 0.7
Potential energy of droplets	4.39 ± 0.02	3.75 ± 0.01
Precipitation	330.1 ± 0.8	296.6 ± 0.8
Sensible heat diffusion	2.04 ± 0.02	2.275 ± 0.008
Total MEP	44 ± 2	39 ± 2

At present, TheDiaTo allows us to perform a thermodynamic analysis of the atmosphere only. However, in principle, it is possible to establish a Lorenz energy cycle also for energy exchanges and transformations within the ocean (von Storch et al. 2013). As high-resolution coupled models now allow for resolutions that are consistent with explicitly resolved mesoscale ocean eddies, a successive development would be creating a set of diagnostics that include the dynamics and thermodynamics of the oceans specifically; this is left for future work.

Acknowledgments. We are grateful to Nicolas Roguet, Anar Artan, Antoine Vandendriessche, Antoine Branca, and Mathieu Fanetti for running some of the MITgcm simulations. We thank anonymous reviewers for very useful remarks that helped in improving the manuscript. The computations were performed on the Baobab cluster at University of Geneva. C. R., C. V., J. K., and M. B. acknowledge the financial support from the Swiss National Science Foundation (Sinergia Project CRSII5_180253). V. Lembo was supported by the Collaborative Research Centre TRR181 ‘Energy Transfers in Atmosphere and Ocean’ funded by the Deutsche Forschungsgemeinschaft (DFG, German Research Foundation), project 274762653. V. Lucarini acknowledges the support provided by the Horizon 2020 project TiPES (Grant 820970).

Data availability statement. The datasets generated during the current study are available from the corresponding author upon request.

APPENDIX

Main Equations Used in TheDiaTo

The goal of this appendix is to remind the reader how to calculate the main quantities discussed in this paper and to describe approximations/adaptations used to apply TheDiaTo on MITgcm outputs. We use (as much as possible) the same notation as Lembo et al. (2019), where the reader can find all the details for the derivation of the equations reported here.

a. Energy budget and transport

Radiative fluxes at the surface (F_s) and at TOA (R_t) depend on latitude ϕ , longitude λ , and time t as follows:

$$F_s(\phi, \lambda, t) = S_s^\downarrow - S_s^\uparrow + L_s^\downarrow - L_s^\uparrow - H_s^\uparrow - H_L^\uparrow, \quad (\text{A1})$$

$$R_t(\phi, \lambda, t) = S_t^\downarrow - S_t^\uparrow - L_t^\uparrow, \quad (\text{A2})$$

where S is shortwave radiation, L longwave radiation, H_L is latent heat flux, and H_s is the sensible heat flux. Subscripts t and s denote top-of-atmosphere and surface, respectively. Upward (\uparrow) or downward (\downarrow) direction is also shown.

Global energy imbalances are computed by averaging F_s and R_t over the total surface and over a period of time of 20 years.

The meridional transport \mathcal{T} is computed by taking the long-term temporal and zonal averages of Eqs. (A1) and (A2), as follows:

$$\mathcal{T}(\phi) = 2\pi \int_{\phi}^{\pi/2} a^2 \cos\phi' < \overline{F(\phi', \lambda, t)} > d\phi', \quad (\text{A3})$$

where F is the radiative flux (at surface, F_s , or at TOA, R_t), a is Earth’s radius, angle brackets represent the long-term time mean, and an overline indicates the zonal mean. The atmospheric transport is computed as the difference between the transport at TOA and that at surface, $\mathcal{T}_{\text{atm}} = \mathcal{T}_{\text{TOA}} - \mathcal{T}_s$.

b. Budget and transport of water-mass and latent heat

The water-mass budget in the atmosphere corresponds to the difference between global averages of surface evaporation and precipitation, $E - P_{\text{tot}}$, where P_{tot} includes both convective and large-scale precipitation. Since rainfall and snowfall precipitations are not differentiated in MITgcm, these are both accounted for within $P_{\text{tot}} = P_r + P_s$.

The evaporation E is an output of MITgcm and its calculation is based on different evaporation coefficients for ocean, land (when it is present), and ice surfaces. Thus, evaporation is not calculated from latent heat as proposed in TheDiaTo [see Eq. (6) in Lembo et al. (2019)].

The meridional water-mass transport is obtained by calculating a cumulative integral over latitude of the zonal mean and long-term time mean of $E - P_{\text{tot}}$, analogously to Eq. (A3).

The latent heat budget R_L depends on the latent heat flux H_L^\uparrow and precipitation P_{tot} :

$$R_L = H_L - L_v P_{\text{tot}}, \quad (\text{A4})$$

where $L_v = 2.5008 \times 10^6 \text{ J kg}^{-1}$ is the latent heat of evaporation. In MITgcm, the latent heat flux is deduced as a residual between the total energy surface budget (an output of MITgcm called TFLUX = F_s) and all the other components [as in Eq. (A1)]. Note that in this way the heat associated with snow melting is taken into account in H_L , assuring in general a well-closed budget also for the latent heat, as shown in Table 1.

c. Material entropy production

To compute the material entropy production, we use the “direct method” of TheDiaTo, where all contributions from irreversible processes are explicitly estimated as follows:

$$\begin{aligned} \text{MEP} = & \underbrace{\int_A \frac{\kappa_s}{T_d} dA}_{\text{Viscous processes}} - \underbrace{\int_A H_s \left(\frac{1}{T_s} - \frac{1}{T_{\text{BL}}} \right) dA}_{\text{Sensible heat diffusion}} - \underbrace{\int_A \frac{L_v E}{T_s} dA}_{\text{Evaporation}} \\ & + \int_{A_r} \left(\underbrace{\frac{L_v P_{\text{tot}}}{T_c}}_{\text{Precipitation}} + g \underbrace{\frac{P_{\text{tot}} h_{\text{ct}}}{T_p}}_{\text{Droplets}} \right) dA_r, \end{aligned} \quad (\text{A5})$$

where T_d is the operating temperature [i.e., mean of near-surface (T_{2m}) and skin temperature (T_s)], T_{BL} is the temperature at the boundary layer, T_c is the working temperature at condensation, T_p is the mean of T_c and T_s , κ_s is the specific kinetic energy dissipation rate, g is the gravitational

acceleration constant, and h_{ct} is the distance covered by droplets. Contributions are integrated over Earth's surface area A or precipitation area A_r . MEP associated with evaporation is directly derived from E given by the MITgcm diagnostics and not from the latent heat.

Note that material entropy production can also be estimated through an "indirect method" separating vertical and horizontal energy transport terms (Lucarini et al. 2011; Lembo et al. 2019). However, we have checked that in MITgcm such an indirect method always overestimates vertical contributions. The low number of atmospheric levels in MITgcm can be the source of this discrepancy with respect to the results obtained with the direct method.

d. Lorenz energy cycle

Storage terms and conversion terms of the LEC are computed in TheDiaTo using formulas given in appendix A of Lembo et al. (2019) or in Ulbrich and Speth (1991). Generation and dissipation terms are computed as residuals of the conversion terms at each reservoir.

e. Horizontal and vertical interpolation

TheDiaTo requires fields on a longitude–latitude grid. Thus we have interpolated the MITgcm output fields from the cubed-sphere grid with 32×32 points per face (corresponding to an average horizontal resolution of 2.8°) to a longitude–latitude grid at 2° .

MITgcm uses an Arakawa C-grid where scalar fields, like temperature and humidity, are saved at the center of grid cells, while vectorial fields are stored at the boundaries. This implies that, while all the scalar quantities and the horizontal components of wind speed are calculated at the centers k , the vertical component is computed at levels $k - 1/2$, with the lowest on the sea surface. Since TheDiaTo requires that all the fields are calculated at the same point, we have linearly interpolated the vertical component of the wind speed on the same levels k as the other quantities. For the upper level (75 hPa), we have used a null vertical component at TOA.

REFERENCES

- Abbot, D. S., A. Voigt, and D. Koll, 2011: The Jormungand global climate state and implications for Neoproterozoic glaciations. *J. Geophys. Res.*, **116**, D18103, <https://doi.org/10.1029/2011JD015927>.
- Adcroft, A., J.-M. Campin, C. Hill, and J. Marshall, 2004: Implementation of an atmosphere ocean general circulation model on the expanded spherical cube. *Mon. Wea. Rev.*, **132**, 2845–2863, <https://doi.org/10.1175/MWR2823.1>.
- Anthes, R. A., 1985: Introduction to parameterization of physical processes in numerical models. *Seminar on Physical Parameterization for Numerical Models of the Atmosphere*, ECMWF, Reading, United Kingdom, Vol. 1, 1–32, <https://www.ecmwf.int/node/7786>.
- Ashwin, P., and A. S. von der Heydt, 2020: Extreme sensitivity and climate tipping points. *J. Stat. Phys.*, **179**, 1531–1552, <https://doi.org/10.1007/s10955-019-02425-x>.
- Balaji, V., and Coauthors, 2017: CPMIP: Measurements of real computational performance of Earth system models in CMIP6. *Geosci. Model Dev.*, **10**, 19–34, <https://doi.org/10.5194/gmd-10-19-2017>.
- Bannon, P. R., 2015: Entropy production and climate efficiency. *J. Atmos. Sci.*, **72**, 3268–3280, <https://doi.org/10.1175/JAS-D-14-0361.1>.
- Becker, E., 2003: Frictional heating in global climate models. *Mon. Wea. Rev.*, **131**, 508–520, [https://doi.org/10.1175/1520-0493\(2003\)131<0508:FHIGCM>2.0.CO;2](https://doi.org/10.1175/1520-0493(2003)131<0508:FHIGCM>2.0.CO;2).
- Benzi, R., G. Parisi, A. Suter, and A. Vulpiani, 1983: A theory of stochastic resonance in climatic change. *SIAM J. Appl. Math.*, **43**, 565–578, <https://doi.org/10.1137/0143037>.
- Boccaletti, G., R. Ferrari, A. Adcroft, D. Ferreira, and J. Marshall, 2005: The vertical structure of ocean heat transport. *Geophys. Res. Lett.*, **32**, L10603, <https://doi.org/10.1029/2005GL022474>.
- Boschi, R., V. Lucarini, and S. Pascale, 2013: Bistability of the climate around the habitable zone: A thermodynamic investigation. *Icarus*, **226**, 1724–1742, <https://doi.org/10.1016/j.icarus.2013.03.017>.
- Brunetti, M., and C. V  rard, 2018: How to reduce long-term drift in present-day and deep-time simulations? *Climate Dyn.*, **50**, 4425–4436, <https://doi.org/10.1007/s00382-017-3883-7>.
- , —, and P. O. Baumgartner, 2015: Modeling the Middle Jurassic ocean circulation. *J. Palaeogeogr.*, **4**, 371–386, <https://doi.org/10.1016/j.jop.2015.09.001>.
- , J. Kasparian, and C. V  rard, 2019: Co-existing climate attractors in a coupled aquaplanet. *Climate Dyn.*, **53**, 6293–6308, <https://doi.org/10.1007/s00382-019-04926-7>.
- Budyko, M. I., 1969: The effect of solar radiation variations on the climate of the Earth. *Tellus*, **21A**, 611–619, <https://doi.org/10.1111/j.2153-3490.1969.tb00466.x>.
- Campin, J.-M., J. Marshall, and D. Ferreira, 2008: Sea ice–ocean coupling using a rescaled vertical coordinate z^* . *Ocean Modell.*, **24** (1), 1–14, <https://doi.org/10.1016/j.ocemod.2008.05.005>.
- Eyring, V., S. Bony, G. A. Meehl, C. A. Senior, B. Stevens, R. J. Stouffer, and K. E. Taylor, 2016: Overview of the Coupled Model Intercomparison Project Phase 6 (CMIP6) experimental design and organization. *Geosci. Model Dev.*, **9**, 1937–1958, <https://doi.org/10.5194/gmd-9-1937-2016>.
- , and Coauthors, 2020: Earth system model evaluation tool (ESMValTool) v2.0—An extended set of large-scale diagnostics for quasi-operational and comprehensive evaluation of Earth system models in CMIP. *Geosci. Model Dev.*, **13**, 3383–3438, <https://doi.org/10.5194/gmd-13-3383-2020>.
- Ferreira, D., J. Marshall, and B. Rose, 2011: Climate determinism revisited: Multiple equilibria in a complex climate model. *J. Climate*, **24**, 992–1012, <https://doi.org/10.1175/2010JCLI3580.1>.
- , —, T. Ito, and D. McGee, 2018: Linking glacial–interglacial states to multiple equilibria of climate. *Geophys. Res. Lett.*, **45**, 9160–9170, <https://doi.org/10.1029/2018GL077019>.
- Ghil, M., 1976: Climate stability for a Sellers-type model. *J. Atmos. Sci.*, **33**, 3–20, [https://doi.org/10.1175/1520-0469\(1976\)033<0003:CSFAST>2.0.CO;2](https://doi.org/10.1175/1520-0469(1976)033<0003:CSFAST>2.0.CO;2).
- , and V. Lucarini, 2020: The physics of climate variability and climate change. *Rev. Mod. Phys.*, **92**, 035002, <https://doi.org/10.1103/RevModPhys.92.035002>.
- Goody, R., 2000: Sources and sinks of climate entropy. *Quart. J. Roy. Meteor. Soc.*, **126**, 1953–1970, <https://doi.org/10.1002/qj.49712656619>.

- Gupta, M., J. Marshall, and D. Ferreira, 2019: Triggering global climate transitions through volcanic eruptions. *J. Climate*, **32**, 3727–3742, <https://doi.org/10.1175/JCLI-D-18-0883.1>.
- Held, I. M., and B. J. Soden, 2006: Robust responses of the hydrological cycle to global warming. *J. Climate*, **19**, 5686–5699, <https://doi.org/10.1175/JCLI3990.1>.
- Hoffman, P. F., A. J. Kaufman, G. P. Halverson, and D. P. Schrag, 1998: A Neoproterozoic snowball earth. *Science*, **281**, 1342–1346, <https://doi.org/10.1126/science.281.5381.1342>.
- Hourdin, F., and Coauthors, 2016: The art and science of climate model tuning. *Bull. Amer. Meteor. Soc.*, **97**, 589–602, <https://doi.org/10.1175/BAMS-D-15-00135>.
- Huber, M., and R. Caballero, 2011: The early Eocene equable climate problem revisited. *Climate Past*, **7**, 603–633, <https://doi.org/10.5194/cp-7-603-2011>.
- Kucharski, F., F. Molteni, and A. Bracco, 2006: Decadal interactions between the western tropical Pacific and the North Atlantic Oscillation. *Climate Dyn.*, **26**, 79–91, <https://doi.org/10.1007/s00382-005-0085-5>.
- , —, M. P. King, R. Farneti, I.-S. Kang, and L. Feudale, 2013: On the need of intermediate complexity general circulation models: A “SPEEDY” example. *Bull. Amer. Meteor. Soc.*, **94**, 25–30, <https://doi.org/10.1175/BAMS-D-11-00238.1>.
- Lauritzen, P. H., and D. L. Williamson, 2019: A total energy error analysis of dynamical cores and physics–dynamics coupling in the Community Atmosphere Model (CAM). *J. Adv. Model. Earth Syst.*, **11**, 1309–1328, <https://doi.org/10.1029/2018MS001549>.
- Lembo, V., D. Folini, M. Wild, and P. Lionello, 2017: Energy budgets and transports: Global evolution and spatial patterns during the twentieth century as estimated in two AMIP-like experiments. *Climate Dyn.*, **48**, 1793–1812, <https://doi.org/10.1007/s00382-016-3173-9>.
- , F. Lunkeit, and V. Lucarini, 2019: TheDiaTo (v1.0)—A new diagnostic tool for water, energy and entropy budgets in climate models. *Geosci. Model Dev.*, **12**, 3805–3834, <https://doi.org/10.5194/gmd-12-3805-2019>.
- Lenton, T. M., H. Held, E. Kriegler, J. W. Hall, W. Lucht, S. Rahmstorf, and H. J. Schellnhuber, 2008: Tipping elements in the Earth’s climate system. *Proc. Natl. Acad. Sci. USA*, **105**, 1786–1793, <https://doi.org/10.1073/pnas.0705414105>.
- Lewis, J. P., A. J. Weaver, and M. Eby, 2007: Snowball versus slushball Earth: Dynamic versus nondynamic sea ice? *J. Geophys. Res.*, **112**, C11014, <https://doi.org/10.1029/2006JC004037>.
- Li, L., A. P. Ingersoll, X. Jiang, D. Feldman, and Y. L. Yung, 2007: Lorenz energy cycle of the global atmosphere based on reanalysis datasets. *Geophys. Res. Lett.*, **34**, L16813, <https://doi.org/10.1029/2007GL029985>.
- Liao, H., C. Wang, and Z. Song, 2021: ENSO phase-locking biases from the CMIP5 to CMIP6 models and a possible explanation. *Deep-Sea Res. II*, **189–190**, 104943, <https://doi.org/10.1016/j.dsr2.2021.104943>.
- Liepert, B. G., and M. Previdi, 2012: Inter-model variability and biases of the global water cycle in CMIP3 coupled climate models. *Environ. Res. Lett.*, **7**, 014006, <https://doi.org/10.1088/1748-9326/7/1/014006>.
- Lorenz, E. N., 1955: Available potential energy and the maintenance of the general circulation. *Tellus*, **7**, 157–167, <https://doi.org/10.3402/tellusa.v7i2.8796>.
- Lucarini, V., 2009: Thermodynamic efficiency and entropy production in the climate system. *Phys. Rev. E*, **80**, 021118, <https://doi.org/10.1103/PhysRevE.80.021118>.
- , and F. Ragone, 2011: Energetics of climate models: Net energy balance and meridional enthalpy transport. *Rev. Geophys.*, **49**, RG1001, <https://doi.org/10.1029/2009RG000323>.
- , and S. Pascale, 2014: Entropy production and coarse graining of the climate fields in a general circulation model. *Climate Dyn.*, **43**, 981–1000, <https://doi.org/10.1007/s00382-014-2052-5>.
- , and T. Bódai, 2017: Edge states in the climate system: Exploring global instabilities and critical transitions. *Nonlinearity*, **30**, R32, <https://doi.org/10.1088/1361-6544/aa6b11>.
- , and —, 2019: Transitions across melancholia states in a climate model: Reconciling the deterministic and stochastic points of view. *Phys. Rev. Lett.*, **122**, 158701, <https://doi.org/10.1103/PhysRevLett.122.158701>.
- , and —, 2020: Global stability properties of the climate: Melancholia states, invariant measures, and phase transitions. *Nonlinearity*, **33**, R59–R92, <https://doi.org/10.1088/1361-6544/ab86cc>.
- , K. Fraedrich, and F. Lunkeit, 2010: Thermodynamic analysis of snowball Earth hysteresis experiment: Efficiency, entropy production and irreversibility. *Quart. J. Roy. Meteor. Soc.*, **136**, 2–11, <https://doi.org/10.1002/qj.543>.
- , —, and F. Ragone, 2011: New results on the thermodynamic properties of the climate system. *J. Atmos. Sci.*, **68**, 2438–2458, <https://doi.org/10.1175/2011JAS3713.1>.
- , R. Blender, C. Herbert, F. Ragone, S. Pascale, and J. Wouters, 2014: Mathematical and physical ideas for climate science. *Rev. Geophys.*, **52**, 809–859, <https://doi.org/10.1002/2013RG000446>.
- Margazoglou, G., T. Grafke, A. Laio, and V. Lucarini, 2021: Dynamical landscape and multistability of a climate model. *Proc. Roy. Soc.*, **A477**, 20210019, <https://doi.org/10.1098/rspa.2021.0019>.
- Marshall, J., and R. A. Plumb, 2008: *Atmosphere, Ocean, and Climate Dynamics: An Introductory Text*. Elsevier, 344 pp.
- , A. Adcroft, C. Hill, L. Perelman, and C. Heisey, 1997a: A finite-volume, incompressible Navier Stokes model for studies of the ocean on parallel computers. *J. Geophys. Res.*, **102**, 5753–5766, <https://doi.org/10.1029/96JC02775>.
- , C. Hill, L. Perelman, and A. Adcroft, 1997b: Hydrostatic, quasi-hydrostatic, and nonhydrostatic ocean modeling. *J. Geophys. Res.*, **102**, 5733–5752, <https://doi.org/10.1029/96JC02776>.
- , A. Adcroft, J.-M. Campin, and C. Hill, 2004: Atmosphere–ocean modeling exploiting fluid isomorphisms. *Mon. Wea. Rev.*, **132**, 2882–2894, <https://doi.org/10.1175/MWR2835.1>.
- Mauritsen, T., and Coauthors, 2012: Tuning the climate of a global model. *J. Adv. Model. Earth Syst.*, **4**, M00A01, <https://doi.org/10.1029/2012MS000154>.
- McKenna, S., A. Santoso, and A. Gupta, 2020: Indian Ocean dipole in CMIP5 and CMIP6: Characteristics, biases, and links to ENSO. *Sci. Rep.*, **10**, 11500, <https://doi.org/10.1038/s41598-020-68268-9>.
- Messori, G., and D. Faranda, 2020: Technical note: Characterising and comparing different palaeoclimates with dynamical systems theory. *Climate Past Discuss.*, **2020**, 1–27, <https://doi.org/10.5194/cp-2020-103>.
- Molteni, F., 2003: Atmospheric simulations using a GCM with simplified physical parametrizations. I: Model climatology and variability in multi-decadal experiments. *Climate Dyn.*, **20**, 175–191, <https://doi.org/10.1007/s00382-002-0268-2>.
- Munk, W., and C. Wunsch, 1998: Abyssal recipes II: Energetics of tidal and wind mixing. *Deep-Sea Res.*, **45**, 1977–2009, [https://doi.org/10.1016/S0967-0637\(98\)00070-3](https://doi.org/10.1016/S0967-0637(98)00070-3).

- Palmer, T. N., 2016: A personal perspective on modelling the climate system. *Proc. Roy. Soc.*, **A472**, 20150772, <https://doi.org/10.1098/rspa.2015.0772>.
- Pascale, S., J. M. Gregory, M. Ambaum, and R. Tailleux, 2011: Climate entropy budget of the HadCM3 atmosphere–ocean general circulation model and of FAMOUS, its low-resolution version. *Climate Dyn.*, **36**, 1189–1206, <https://doi.org/10.1007/s00382-009-0718-1>.
- Pauluis, O., 2007: Sources and sinks of available potential energy in a moist atmosphere. *J. Atmos. Sci.*, **64**, 2627–2641, <https://doi.org/10.1175/JAS3937.1>.
- , and I. M. Held, 2002: Entropy budget of an atmosphere in radiative–convective equilibrium. Part II: Latent heat transport and moist processes. *J. Atmos. Sci.*, **59**, 140–149, [https://doi.org/10.1175/1520-0469\(2002\)059<0140:EBOAAI>2.0.CO;2](https://doi.org/10.1175/1520-0469(2002)059<0140:EBOAAI>2.0.CO;2).
- Peixoto, J. P., and A. H. Oort, 1992: *Physics of Climate*. AIP Press, 512 pp.
- Perkins, S. E., 2011: Biases and model agreement in projections of climate extremes over the tropical Pacific. *Earth Interact.*, **15**, <https://doi.org/10.1175/2011EI395.1>.
- Pierrehumbert, R., D. Abbot, A. Voigt, and D. Koll, 2011: Climate of the Neoproterozoic. *Ann. Rev. Earth Planet. Sci.*, **39**, 417–460, <https://doi.org/10.1146/annurev-earth-040809-152447>.
- Pohl, A., Y. Donnadieu, G. Le Hir, J.-F. Buoncristiani, and E. Vennin, 2014: Effect of the Ordovician paleogeography on the (in)stability of the climate. *Climate Past*, **10**, 2053–2066, <https://doi.org/10.5194/cp-10-2053-2014>.
- Popp, M., H. Schmidt, and J. Marotzke, 2016: Transition to a moist greenhouse with CO₂ and solar forcing. *Nat. Commun.*, **7**, 10627, <https://doi.org/10.1038/ncomms10627>.
- Rausser, F., P. Gleckler, and J. Marotzke, 2015: Rethinking the default construction of multimodel climate ensembles. *Bull. Amer. Meteor. Soc.*, **96**, 911–919, <https://doi.org/10.1175/BAMS-D-13-00181.1>.
- Rose, B. E. J., 2015: Stable ‘WaterBelt’ climates controlled by tropical ocean heat transport: A nonlinear coupled climate mechanism of relevance to Snowball Earth. *J. Geophys. Res. Atmos.*, **120**, 1404–1423, <https://doi.org/10.1002/2014JD022659>.
- , D. Ferreira, and J. Marshall, 2013: The role of oceans and sea ice in abrupt transitions between multiple climate states. *J. Climate*, **26**, 2862–2879, <https://doi.org/10.1175/JCLI-D-12-00175.1>.
- Saltzman, B., 2001: *Dynamical Paleoclimatology: Generalized Theory of Global Climate Change*. Elsevier, 354 pp.
- Seager, S., 2013: Exoplanet habitability. *Science*, **340**, 577–581, <https://doi.org/10.1126/science>.
- Sellers, W. D., 1969: A global climatic model based on the energy balance of the Earth–atmosphere system. *J. Appl. Meteor.*, **8**, 392–400, [https://doi.org/10.1175/1520-0450\(1969\)008<0392:AGCMBO>2.0.CO;2](https://doi.org/10.1175/1520-0450(1969)008<0392:AGCMBO>2.0.CO;2).
- Stone, P. H., 1978: Constraints on dynamical transports of energy on a spherical planet. *Dyn. Atmos. Oceans*, **2**, 123–139, [https://doi.org/10.1016/0377-0265\(78\)90006-4](https://doi.org/10.1016/0377-0265(78)90006-4).
- Stouffer, R. J., V. Eyring, G. A. Meehl, S. Bony, C. Senior, B. Stevens, and K. E. Taylor, 2017: CMIP5 scientific gaps and recommendations for CMIP6. *Bull. Amer. Meteor. Soc.*, **98**, 95–105, <https://doi.org/10.1175/BAMS-D-15-00013.1>.
- Trenberth, K. E., 2020: Understanding climate change through Earth’s energy flows. *J. Roy. Soc. NZ*, **50**, 331–347, <https://doi.org/10.1080/03036758.2020.1741404>.
- , J. T. Fasullo, and J. Kiehl, 2009: Earth’s global energy budget. *Bull. Amer. Meteor. Soc.*, **90**, 311–324, <https://doi.org/10.1175/2008BAMS2634.1>.
- Ulrich, U., and P. Speth, 1991: The global energy cycle of stationary and transient atmospheric waves: Results from ECMWF analyses. *Meteor. Atmos. Phys.*, **45**, 125–138, <https://doi.org/10.1007/BF01029650>.
- Veiga, J. A. P., and T. Ambrizzi, 2013: A global and hemispherical analysis of the Lorenz energetics based on the representative concentration pathways used in CMIP5. *Adv. Meteor.*, **2013**, 485047, <https://doi.org/10.1155/2013/485047>.
- von der Heydt, A. S., and P. Ashwin, 2017: State dependence of climate sensitivity: Attractor constraints and palaeoclimate regimes. *Dyn. Stat. Climate Syst.*, **1**, dx001, <https://doi.org/10.1093/climsys/dzx001>.
- von Storch, J.-S., C. Eden, I. Fast, H. Haak, D. Hernández-Deckers, E. Maier-Reimer, J. Marotzke, and D. Stammer, 2013: An estimate of the Lorenz energy cycle for the World Ocean based on the STORM/NCEP simulation. *J. Phys. Oceanogr.*, **42**, 2185–2205, <https://doi.org/10.1175/JPO-D-12-079.1>.
- Wang, C., L. Zhang, S. Lee, L. Wu, and C. R. Mechoso, 2014: A global perspective on CMIP5 climate model biases. *Nat. Climate Change*, **4**, 201–205, <https://doi.org/10.1038/nclimate2118>.
- Wild, M., 2020: The global energy balance as represented in CMIP6 climate models. *Climate Dyn.*, **55**, 553–577, <https://doi.org/10.1007/s00382-020-05282-7>.
- Winton, M., 2000: A reformulated three-layer sea ice model. *J. Atmos. Oceanic Technol.*, **17**, 525–531, [https://doi.org/10.1175/1520-0426\(2000\)017<0525:ARTLSI>2.0.CO;2](https://doi.org/10.1175/1520-0426(2000)017<0525:ARTLSI>2.0.CO;2).
- Wunsch, C., and R. Ferrari, 2004: Vertical mixing, energy, and the general circulation of the oceans. *Ann. Rev. Fluid Mech.*, **36**, 281–314, <https://doi.org/10.1146/annurev.fluid.36.050802.122121>.
- Yang, Y., S.-P. Xie, L. Wu, Y. Kosaka, and J. Li, 2018: ENSO forced and local variability of north tropical Atlantic SST: Model simulations and biases. *Climate Dyn.*, **51**, 4511–4524, <https://doi.org/10.1007/s00382-017-3679-9>.
- Zhang, X., H. Liu, and M. Zhang, 2015: Double ITCZ in coupled ocean–atmosphere models: From CMIP3 to CMIP5. *Geophys. Res. Lett.*, **42**, 8651–8659, <https://doi.org/10.1002/2015GL065973>.